



Simulations of galaxy cluster mergers with velocity-dependent, rare, and frequent self-interactions

V. M. Sabarish ¹★, Marcus Brüggen ¹, Kai Schmidt-Hoberg ², Moritz S. Fischer ^{3,4} and Felix Kahlhoefer ⁵

¹Hamburger Sternwarte, Universität Hamburg, Gojenbergsweg 112, D-21029 Hamburg, Germany

²Deutsches Elektronen-Synchrotron DESY, Notkestr. 85, D-22607 Hamburg, Germany

³Universitäts-Sternwarte, Fakultät für Physik, Ludwig-Maximilians-Universität München, Scheinerstr. 1, D-81679 München, Germany

⁴Excellence Cluster ORIGINS, Boltzmannstrasse 2, D-85748 Garching, Germany

⁵Institute for Theoretical Particle Physics (TTP), Karlsruhe Institute of Technology (KIT), D-76128 Karlsruhe, Germany

Accepted 2024 February 28. Received 2024 February 6; in original form 2023 September 30

ABSTRACT

Self-interacting dark matter (SIDM) has been proposed to solve small-scale problems in Λ CDM cosmology. In previous work, constraints on the self-interaction cross-section of dark matter have been derived assuming that the self-interaction cross-section is independent of velocity. However, a velocity-dependent cross-section is more natural in most theories of SIDM. Using idealized N -body simulations without baryons, we study merging clusters with velocity-dependent SIDM. In addition to the usual rare scattering in the isotropic limit, we also simulate these systems with anisotropic, small-angle (frequent) scatterings. We find that the collisionless brightest cluster galaxy (BCG) has an offset from the DM peak that grows at later stages. Finally, we also extend the existing upper bounds on the velocity-independent, isotropic self-interaction cross-section to the parameter space of rare and frequent velocity-dependent self-interactions by studying the central densities of dark matter-only isolated haloes. For these upper-bound parameters, the DM-BCG offsets just after the first pericentre in the dark matter-only simulations are found to be $\lesssim 10$ kpc. On the other hand, because of BCG oscillations, we speculate that the distribution of BCG offsets in a relaxed cluster is a statistically viable probe. Therefore, this motivates further studies of BCG off-centring in hydrodynamic cosmological simulations.

Key words: astroparticle physics – methods: numerical – dark matter.

1 INTRODUCTION

Cold dark matter (CDM) is a fundamental component of the standard Λ CDM cosmology. It plays a vital role in explaining the formation of the large-scale structure of the Universe and the anisotropies in the cosmic microwave background. While cosmological N -body simulations within Λ CDM have successfully reproduced many observations of the large-scale structure, there seem to be discrepancies between observations and simulations on small scales (see Bullock & Boylan-Kolchin 2017 for a review of the small-scale problems). A solution to the small-scale problems was proposed by Spergel & Steinhardt (2000) via a model of DM, where DM particles can non-gravitationally scatter off each other. Constraints on the self-interaction cross-section can be obtained by studying different astrophysical systems. In particular, relaxed galaxy clusters (e.g. Andrade et al. 2021; Sagunski et al. 2021) have provided the most stringent constraint on the cross-section. We also have constraints from galaxy cluster mergers (Randall et al. 2008; Harvey et al. 2015). For a review on astrophysical constraints on self-interacting dark matter (SIDM) see Adhikari et al. (2022).

Velocity-dependent anisotropic cross-sections are natural in most theories of SIDM (for a review of SIDM models see Tulin & Yu 2018). Examples of such models include light mediator models (Ackerman et al. 2009; Tulin, Yu & Zurek 2013), atomic DM (Cline et al. 2014), strongly interacting DM (Boddy et al. 2014). Moreover, velocity-dependent cross-sections are also well motivated observationally. Most constraints on the self-interaction cross-section per unit mass of DM particle (σ/m_χ) in the literature, have been derived assuming velocity-independent and isotropic scattering. For example, Sagunski et al. (2021) quote an upper limit of $\sigma/m_\chi < 0.35 \text{ cm}^2 \text{ g}^{-1}$ (95 per cent C.L.) at cluster scales and $\sigma/m_\chi < 1.1 \text{ cm}^2 \text{ g}^{-1}$ (95 per cent C.L.) at group scales. On the galactic scales, Ren et al. (2019) find that σ/m_χ is required to be in the range 3–10 $\text{cm}^2 \text{ g}^{-1}$ to explain the observed diversity in the rotation curves in the SPARC data set. Similarly, Sankar Ray, Sarkar & Kumar Shaw (2022) quote an upper-bound of $\sigma/m_\chi < 9.8 \text{ cm}^2 \text{ g}^{-1}$ (95 per cent C.L.). At the scale of dwarf galaxies, there is no concrete upper bound on the cross-section. A cross-section with $\sigma/m_\chi > 30 \text{ cm}^2 \text{ g}^{-1}$ is favoured by the observed central densities of Milky Way’s dwarf spheroidal galaxies (Correa 2021). Elbert et al. (2015) find that σ/m_χ can be as large as 50 $\text{cm}^2 \text{ g}^{-1}$ at these scales and still be consistent with observations. These considerations highlight the viability of velocity-dependent cross-sections.

* E-mail: sabarish.venkataramani@uni-hamburg.de

Observationally probing the angular dependence is a daunting task. One reason being that the effects of angular dependence are not strong enough when studying the evolution of systems that do not have a preferred direction. For example, Robertson, Massey & Eke (2017b) and Fischer et al. (2021) simulated isolated haloes using N -body simulations and found that there is no big difference in the evolution of core-sizes between isotropic and anisotropic cross-sections for a given choice of parameters. Moreover, simulating differential cross-sections which peak for tiny scattering angles, using conventional SIDM implementations (e.g. Rocha et al. 2013) is prohibitively expensive. This type of interaction will be called frequent self-interactions (as introduced in Kahlhoefer et al. 2014) as opposed to rare self-interactions corresponding to large-angle scattering. Frequently self-interacting dark matter (fSIDM) is natural in the mass-less mediator limit of light mediator models. The scattering of DM particles in this regime can be modelled as a drag force, where the drag force depends not on the total cross-section but on the momentum transfer cross-section given by Kahlhoefer, Schmidt-Hoberg & Wild (2017) and Robertson, Massey & Eke (2017b)

$$\sigma_T = 2\pi \int_{-1}^1 \frac{d\sigma}{d\Omega_{\text{cms}}} (1 - |\cos \theta_{\text{cms}}|) d \cos \theta_{\text{cms}}, \quad (1)$$

where θ_{cms} and Ω_{cms} are the scattering angle, and solid angle in the centre of mass frame. Frequent self-interactions have previously been studied by Kahlhoefer et al. (2014), Kummer, Kahlhoefer & Schmidt-Hoberg (2018), Kummer et al. (2019), and Fischer et al. (2021, 2022) assuming velocity independence.

Mergers of galaxy clusters are interesting test beds for models of SIDM since the mass distribution of the system could be measured through lensing. The gas and galaxies can be probed through their direct emission in various wavelengths. The existence of offsets between the DM component and galaxies may hint at DM self-interactions (Randall et al. 2008). Moreover, mergers are sensitive to both velocity and angular dependence of the scattering cross-section. First, as the haloes undergo many pericentre passages, the collisional velocity changes with time. Scattering velocities are the largest at the first pericentre passage and, subsequently, the haloes slow down with every passage. The self-interactions at the pericentre passages are mainly responsible for an increase in the offset. Thus, the evolution is sensitive to the parameters of velocity-dependent cross-section. Secondly, mergers unlike isolated haloes also have a preferred direction, i.e. the merger axis. Fischer et al. (2022) find that offsets are larger for frequent self-interactions with a given σ_T , when compared to rare self-interactions of the same σ_T . They also showed that small-angle scattering can produce larger offsets than the maximal possible offset from isotropic scattering.

There have been earlier studies that have simulated mergers. For example, studies with velocity-independent isotropic cross-sections have been done by Kim, Peter & Wittman (2017) who simulated equal-mass mergers; Robertson, Massey & Eke (2017a) simulated a bullet cluster like system. Fischer et al. (2021, 2022) studied equal and unequal-mass mergers with isotropic and anisotropic velocity-independent cross-sections. Robertson, Massey & Eke (2017b) looked at mergers until just after the first pericentre passage. They used a velocity-dependent isotropic cross-section and a velocity-dependent cross-section that corresponds to Yukawa scattering under the Born approximation. It is unknown as to how the merger evolution is affected at late stages by velocity-dependent self-interactions. Similarly, mergers in the fSIDM regime with velocity dependence are yet to be studied.

In this work, we aim to (i) study the qualitative differences in merger simulations between velocity-dependent and independent

cross-sections, (ii) extend the upper bound on constant cross-section quoted by Sagunski et al. (2021) to the parameter space of velocity-dependent cross-section, (iii) find the maximum offsets between DM and the brightest cluster galaxy (BCG) with velocity-dependent cross-section parameters that are consistent with upper bound parameters. To this end, we simulate the full evolution of galaxy cluster mergers and isolated haloes with rare and frequent self-interactions. In a companion paper (Fischer et al. 2024), cosmological simulations are studied with velocity-dependent fSIDM. The paper is presented as follows. In Section 2 we briefly describe our numerical scheme and the SIDM models that are considered. In Section 3 we present our simulation results, which illustrate the qualitative differences between velocity-dependent and velocity-independent cross-section simulations. In Section 4, we describe the simulations of mergers with cross-section parameters that correspond to the 95 per cent C.L. limits provided in Sagunski et al. (2021). In Section 5, we summarize our results and conclude. Additional details are provided in the Appendices A and B.

2 METHODS

In this section, we describe the numerical setup of our simulations, and we discuss our choice for the self-interaction cross-section that is used in the simulations.

2.1 Numerical method

For our simulations, we use the cosmological N -body simulation code OPENGADGET3, adapted for frequent self-interactions using the implementation given in Fischer et al. (2021). In this section, we briefly describe the implementation of rare and frequent self-interactions. The numerical scheme for the self-interactions of rarely self-interacting dark matter (rSIDM) follows Fischer et al. (2021), which is similar to the method described in Rocha et al. (2013). In this scheme, the probability that a numerical particle 1 with mass m_1 scatters off another numerical particle 2 with mass m_2 is given by,

$$P_{12} = \frac{\sigma(v_{12})}{m_\chi} m_2 ||v_{12}|| \Delta t \Lambda_{12}, \quad (2)$$

where v_{12} is the relative velocity between the numerical particles 1 and 2, Δt is the time-step used in the simulation, Λ_{12} is the kernel overlap integral, $\sigma(v_{12})/m_\chi$ is the total cross-section per unit mass of DM particle. For more details on the implementation and the choice for the kernel, see appendix A and B of Fischer et al. (2021). A collection of kernels used in other modern implementations of SIDM within N -body simulations can be found in Adhikari et al. (2022, equations 11–15).

The drag force of frequent self-interactions is based on the relation derived in Kahlhoefer et al. (2014), which describes the deceleration rate experienced by a particle as it travels through a constant background density of DM,

$$R_{\text{dec}} = \frac{1}{v_0} \frac{dv_{\parallel}}{dt} = \frac{\rho_0 v_0 \sigma_T}{2m_\chi}, \quad (3)$$

v_0 is the velocity of the particle, v_{\parallel} is the parallel component of the velocity of the particle, ρ_0 is the background density, σ_T is the momentum transfer cross-section defined in equation (1). We can also see that the deceleration rate captures the rate of change of the parallel component of the velocity. Therefore, the above expression can then be cast into an expression for drag force for the physical particles. The drag force as experienced by numerical particles, labelled 1 and

2, in the N -body code is given as (Fischer et al. 2021),

$$F_{\text{drag}} = \frac{1}{2} |v_{12}|^2 \frac{\sigma_{\text{T}}(v_{12})}{m_{\chi}} m_1 m_2 \Lambda_{12}, \quad (4)$$

which is proportional to the momentum transfer cross-section σ_{T} . From here on, we will drop the subscripts and let v denote the relative velocity between DM particles.

In addition to the drag force, momentum is added to the particles in a random but perpendicular direction relative to the motion in the centre-of-mass frame. As for rSIDM, the post-scattered momenta in the centre-of-mass frame have the same absolute value as the pre-scattered ones.

In our SIDM implementation, we search for pairs of potentially interacting particles. A search for the neighbours of each particle achieves this, employing the same tree structure as used in the gravity computation.

The code employs an adaptive time-stepping scheme, where the time-step of an individual particle is obtained by the minimum of different time-step criteria, i.e. given by gravity and self-interactions.

The implementation of rSIDM and fSIDM does conserve momentum as well as energy explicitly. This is achieved by executing the scattering computations for pairs of particles in a consecutive manner such that their velocities are updated after each scattering event and used for the next one. At the same time, we allow for multiple interactions per particle per time-step.

Massively parallel computations of the self-interactions are enabled by a parallelized implementation using the message passing interface (MPI). Note, here we order the communication and computation of the processes in a manner to reduce waiting time.

The implementation of the velocity-dependent self-interactions into the SIDM module has been described in detail by Fischer et al. (2024). To ensure numerically stable results, a novel time-step criterion has been added. This criterion is based on the velocity at which self-interactions are strongest, i.e. on the maximum of $\sigma_{\text{T}}(v) v$, instead of the velocity distribution that an individual particle encountered in the previous time-step. In principle, such a scheme guarantees that the simulation time-step is always sufficiently small to account for $\sigma_{\text{T}}(v)$ for any v .

2.2 Initial conditions and simulation parameters

In this work, we simulate both DM-only isolated haloes and galaxy cluster merger with two different merger mass ratios (MMR). First for the isolated DM-only haloes, they have a virial mass of $1 \times 10^{15} M_{\odot}$ and are initialized with an NFW density profile Navarro, Frenk & White (1996), i.e.

$$\rho(r) = \frac{\delta_c \rho_{\text{crit}}}{(r/r_s)(1+r/r_s)^2} := \frac{\rho_0}{(r/r_s)(1+r/r_s)^2}. \quad (5)$$

DM positions are sampled from a probability density function such that the density profile follows the NFW profile. Given the virial mass of the halo and the critical density ρ_{crit} of the universe, the parameters of the NFW profile are determined as follows: (i) the concentration parameter c_{vir} is determined using the concentration–mass relation given in Dutton & Macciò (2014), (ii) characteristic density δ_c is computed using c_{vir} from the earlier step (using equation 2 of Navarro, Frenk & White 1996), (iii) scale radius r_s is computed using its definition $r_s = r_{\text{vir}}/c_{\text{vir}}$. The NFW parameters thus obtained are given in Table 1. Using the resulting density profile, the initial velocity dispersion $\langle v^2 \rangle_{\text{ini}}(r)$ is obtained by integrating the Jeans equation (Binney & Tremaine 2008). Then, initial velocities in each radial bin are drawn from a Gaussian distribution with the variance

Table 1. This table contains the NFW parameters used in generating the ICs for merger simulations. The first column contains the virial mass, the second the density parameter $\rho_0 := \delta_c \rho_{\text{crit}}$, followed by scale radius r_s , concentration parameter and number of DM and galaxy particles. DM-only isolated haloes have the same NFW parameters as given in the first row.

M_{vir} (M_{\odot})	ρ_0 ($M_{\odot} \text{kpc}^{-3}$)	r_s (kpc)	c	$N_{\text{DM}} = N_{\text{Gal}}$	N_{BCG}
10^{15}	1.33×10^6	389.3	5.42	1 009 878	1
2×10^{14}	1.908×10^6	194.76	6.33	181 319	1

Table 2. This table contains the initial separation, initial relative velocity between the two clusters, and the relative velocity of the BCGs at the first pericentre passage.

Merger mass ratios ($M_{\odot} : M_{\odot}$)	x_{ini} (kpc)	Δv_{ini} (km s^{-1})	$\Delta v_{\text{BCG}}^{\text{(BCG)}}$ (km s^{-1})
$10^{15} : 10^{15}$	4000	1000	5500
$10^{15} : 2 \times 10^{14}$	4000	1000	4800

$\langle v^2 \rangle_{\text{ini}}(r)$. The isolated DM halo simulations use the same NFW parameters as the main halo of the merger for initial conditions (ICs). We simulate mergers with $\text{MMR} \in \{1, 5\}$. The barycentre of the clusters are initially 4000 kpc apart and they are put on course towards each other with a relative velocity of 1000 km s^{-1} as summarized in Table 2.

In the galaxy cluster used in the merger simulations, the cluster has three particle species: DM, galaxy, and BCG. Galaxies and BCG are approximated to be collision-less, while DM is collisional with self-interaction characterized by its cross-section. An equal number of DM and galaxy particles is used in the simulation. A sufficient number of galaxy particles are chosen to ensure that it is easier to find the peak position of the galaxies. The main halo has a virial mass of $10^{15} M_{\odot}$ and both species initially follow an NFW profile. The particle masses are as follows: for DM, $m_{\text{DM}} = 2 \times 10^9 M_{\odot}$, for galaxies, $m_{\text{Gal}} = 4 \times 10^7 M_{\odot}$. In addition, the brightest cluster galaxy (BCG) is represented by a single particle at the centre of the halo with a mass $m_{\text{BCG}} = 7 \times 10^{11} M_{\odot}$. As the BCG is approximated to be a point particle, the effects of gravitational scattering become strong if the mass is large, therefore the BCG particle is taken to be less massive than the observed BCGs. This choice is adopted from earlier studies (e.g. Kim, Peter & Wittman 2017; Fischer et al. 2022). The mass resolution chosen works reasonably well for measuring offsets in simulation since the simulation is run only for a few dynamical time-scales. The detailed effects of such a treatment on measurements other than offsets are yet to be studied. We use a fixed gravitational softening length of $\epsilon = 1.2 \text{ kpc}$ for all particles. For both mergers and isolated haloes we use an adaptive kernel size for the DM self-interactions, such that the number of neighbours within each particles' kernel, N_{ngb} is equal to 64. This choice follows from Fischer et al. (2021).

All simulations have been performed with a resolution of $\mathcal{O}(10^6)$ particles. For certain cross-section parameters, the simulations were rerun at a higher resolution of $\mathcal{O}(10^7)$ particles to validate the lower resolution runs (see Appendix A).

2.3 Dark matter cross-section model

We assume a fairly generic form for the self-interaction momentum transfer cross-section for rare and frequent self-interactions,

parametrized as follows (Gilman et al. 2021; Yang et al. 2023),

$$\frac{\sigma_T(v)}{m_\chi} = \frac{\sigma_0}{m_\chi} \left(1 + \frac{v^2}{w^2}\right)^{-2}, \quad (6)$$

where v is the relative velocity of the DM particles. We furthermore assume that the total cross-section has the same velocity dependence as the momentum transfer cross-section, such that

$$\frac{\sigma_T(v)}{\sigma_T(v=0)} = \frac{\sigma(v)}{\sigma(v=0)}. \quad (7)$$

This assumption is automatically satisfied if the differential cross-section is a separable function, i.e. it is of the following form,

$$\frac{d\sigma}{d\cos\theta} = N \frac{\sigma_0}{m_\chi} \Theta(\theta) g(w, v), \quad (8)$$

where N is a normalization constant, $\Theta(\theta)$ captures the angular dependence and $g(w, v) = (1 + v^2/w^2)^{-2}$. However, even for non-separable differential cross-sections, such as Rutherford scattering, the assumption in equation (7) gives a useful approximation.

Depending on the choice of N and $\Theta(\theta)$, the above differential cross-section can correspond to either frequent or rare self-interactions. In this work, we consider isotropic scattering for the case of rare self-interactions, such that $\Theta(\theta)$ is simply a number. The total cross-section to calculate the scattering probability in equation (2) is then given by $\sigma(v) = 2\sigma_T(v)$, see equation (1). For frequent self-interactions, on the other hand, $\Theta(\theta)$ is strongly peaked for small angles. The normalization, N , is then chosen such that the momentum transfer cross-section given in equation (6) is recovered, which is used in the simulations to compute the drag force experienced by the particles, see equation (4).

To run the simulations, the parameters σ_{0m} and w must be chosen, where $\sigma_{0m} := \sigma_0/m_\chi$. In this paper, we are interested in studying the qualitative differences in the evolution of galaxy cluster mergers between the different regions of $\sigma_{0m} - w$ parameter space. A priori, it is conceivable that there are degeneracies in this parameter space, such that different parameter combinations lead to very similar merger observables. Such a degeneracy was found by Yang et al. (2023) (see their fig. 8) when analysing the rotation curve of LSB dwarf galaxy UGC 128. In other words, it was possible to compensate a change in w by an appropriate change in σ_{0m} . We refer to a prescription to determine the cross-section normalization σ_{0m} for a given velocity dependence (determined by w) as *matching*. In the following, we will explore different matching procedures.

The choice for w follows from the typical relative velocity scales. These scales can be estimated by running CDM simulations. The observed values are displayed as dashed lines in Fig. 1. The largest observed scales are the relative velocities of the infalling BCGs shown as the last two lines corresponding to MMR:5 and MMR:1, respectively. The average scattering velocity with which DM particles scatter off each other within 100 kpc around the barycentre at the first pericentre passage are shown. Finally, the relative velocity dispersion within 100 kpc of a $1 \times 10^{15} M_\odot$ halo is displayed as the leftmost vertical dashed line and it is approximately 1400 km s^{-1} . This implies that for any value of w larger than 1400 km s^{-1} , the self-interactions within the halo will be in the weakly velocity-dependent regime. Therefore, the following choice for w is made, $w \in \{1000, 2000, 3000, 4000\} \text{ km s}^{-1}$.

We have analysed cluster mergers with σ_{0m} chosen according to two matching procedures: The first is to choose the same value of σ_{0m} for all chosen values of w , the second is to choose σ_{0m} such that the evolution of the central density of the isolated haloes for different

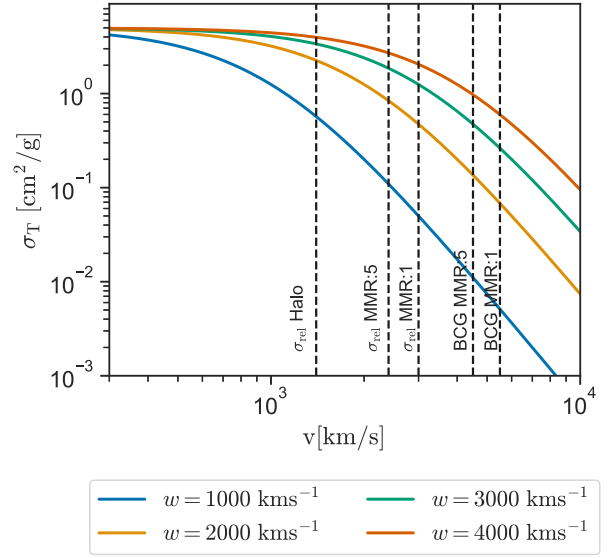


Figure 1. Momentum transfer cross-section for $\sigma_{0m} = 5 \text{ cm}^2 \text{ g}^{-1}$, and the values of w are given in the legend. The vertical coloured dashed lines correspond to different velocity scales in the system. The left most is the relative velocity dispersion within 100 kpc of the $1 \times 10^{15} M_\odot$ cluster. The second and third from the left correspond to the relative velocity dispersion within 100 kpc around the barycentre at the first pericentre for MMR:5 and MMR:1, respectively. Finally, the second last and the last are the relative velocity of the BCGs at the first pericentre passage of the system with MMR:5 and MMR:1, respectively.

values of w is similar. These procedures will be explained further in the following sections.

2.4 Analysis methods

In order to find the peak position of any component, i.e. DM or galaxies, we use the peak finding method based on the gravitational potential, see Fischer et al. (2022). In the simulations, all particles have a unique particle ID assigned to them. Using the ID, particles belonging to a given halo can be identified. Then, the gravitational potential in each cell in a grid is computed. The cell with the lowest potential corresponds to the position of the peak. Fischer et al. (2022) also propose the isodensity-based peak finding algorithm. In this algorithm, the peaks are identified as the cell in the merger plane with the highest projected density. This method is closer to observations where, for example, gravitational shear measurements can be used to infer mass densities. We find that gravitational potential based peak finding is more reliable when the simulation is run with low resolution. Hence, this is our choice for finding peaks. To find the errors on the peak position, we bootstrap the particle distribution 20 times and determine 20 such peaks. Then we estimate the error, by finding the standard deviation in the obtained peak positions.

We define offsets as the distance between the peaks of two different species of the same cluster. For example, $d_{\text{DM-BCG}}$ is the distance between the DM and BCG peak of a given cluster.

3 VARYING w ONLY

In this scheme, the same value of σ_{0m} is used for different values of the parameter w . Even though it is a very simple choice, it is easier to observe the qualitative difference introduced by velocity-dependent cross-sections. To make the differences stand out, we use

Table 3. Simulation labels and the corresponding cross-section parameters. The generic form of labels is $XwDsNpM$, where X is F(frequent), R(rare), or C(constant). D that follows w is the value of the parameter w to be read as $D \text{ km s}^{-1}$ and NpM following the s is the value of σ_{0m} to be read as $N.M \text{ cm}^2 \text{ g}^{-1}$.

Simulation name	$\sigma_{0m} (\text{cm}^2 \text{g}^{-1})$	$w (\text{km s}^{-1})$
FC5p0	5	∞
Fw1000s5p0	5	1000
Fw2000s5p0	5	2000
Fw3000s5p0	5	3000
Fw4000s5p0	5	4000

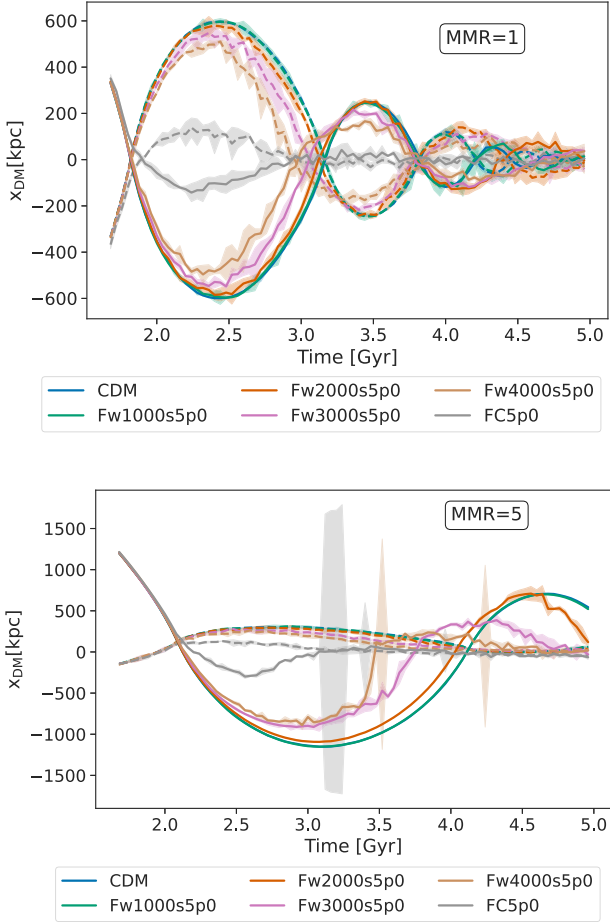


Figure 2. The dotted and solid lines correspond to the DM peak position of the main halo and subhalo, respectively. Upper panel: DM peaks in equal-mass merger, lower panel: Merger with mass ratio 5. Plot labels are described in Table 3. Simulation results presented in this figure corresponds to varying values of w and a fixed σ_{0m} .

a large value of $\sigma_{0m} = 5.0 \text{ cm}^2 \text{ g}^{-1}$. We confirmed the results to be qualitatively similar but less pronounced for smaller values of σ_{0m} . The names for the individual runs shown in the plots are tabulated in Table 3.

3.1 DM peak position

The plots of the peak positions of DM against time for equal and unequal-mass mergers are given in Fig. 2. The peaks of the main halo are marked by dotted lines, while those of subhalo are indicated by

solid lines. First, we observe that for constant σ_T the drag force from self-interaction is strong enough to stop the DM component in their tracks and they coalesce at the first pericentre passage. For the same σ_{0m} , the DM peak positions in the velocity-dependent SIDM runs are closer to the CDM run for smaller values of w . This observation matches our expectation that, for fixed σ_{0m} , increasing w increases the effective self-interaction strength.

The separation of the peaks at the first apocentre is largest for CDM and decreases with increasing self-interaction strength. This can be attributed to the fact that DM particles experience a drag force and thus stay closer to the centre-of-mass of the system.

The first pericentre passage occurs at different times for different parameter combinations. Albeit a small effect, self-interactions tend to increase the time taken to reach the first pericentre passage. Then the second passage occurs earlier for increasing self-interaction strength. For example, we see that the first pericentre passage occurs slightly later in the simulation with constant σ_T . This could be understood as self-interactions generating pressure that resists the infall, thus slowing the halo down. The difference is large for constant σ_T because the effective self-interaction strength of the velocity-dependent ones is much smaller than the one of constant σ_T at early stages, as $\sigma_T(v)$ is small for $v > w$.

At later stages of the evolution, the scenario changes. For example, at the third apocentre, we see that the oscillation in the DM peak for $w = 2000 \text{ km s}^{-1}$ has an amplitude that is greater than that of CDM. During these stages, the central density of the haloes are lower for SIDM simulations (see Fig. C2). Therefore, the oscillations are less dampened by dynamical friction for SIDM simulations.

For the unequal-mass mergers, the subhalo dissolves faster, making it difficult to identify the DM peaks during later stages of the evolution. Both equal and unequal mass mergers have identical initial separation and initial relative velocity. Therefore, in unequal mass merger, the less massive cluster traverses more distance than the massive one and this leads to fewer oscillations. For instance, in Fig. 2, we see that within 5 billion years, the subhalo in MMR:5 system has undergone fewer pericentre passages than the equal-mass merger.

3.2 BCG peak position

The BCG positions for subhaloes are given in Fig. 3, the upper panel corresponds to the equal-mass merger system, while the lower panel corresponds to the unequal-mass merger. In CDM simulations, the BCG oscillations are damped faster compared to SIDM simulations. This general feature has already been observed in earlier work (Kim, Peter & Wittman 2017; Fischer et al. 2021, 2022). This could be explained by noting that the merger remnants have a cored density distribution at the centre owing to the self-interactions. On the other hand, merger remnants in CDM simulations have larger central densities. As a result, the oscillations dampen out faster in CDM due to dynamical friction.

In the equal-mass merger, we observe that the peak positions of subhalo BCGs are closer to the CDM for smaller values of w at the early stages of the merger evolution. At later stages, around 5 billion years, the BCG oscillations in the CDM simulation have dampened considerably. On the other hand, the oscillations approximately stay constant for the constant σ_T simulation for the period 1–8 billion years, as shown in Fig. 3. The position of the BCG in velocity-dependent simulations start deviating from CDM with time. For example, let us consider the $w = 2000 \text{ km s}^{-1}$ simulation: (i) we see that the curve is initially close to the CDM simulation (ii) during the period 4–7 billion years, the oscillations have approximately a

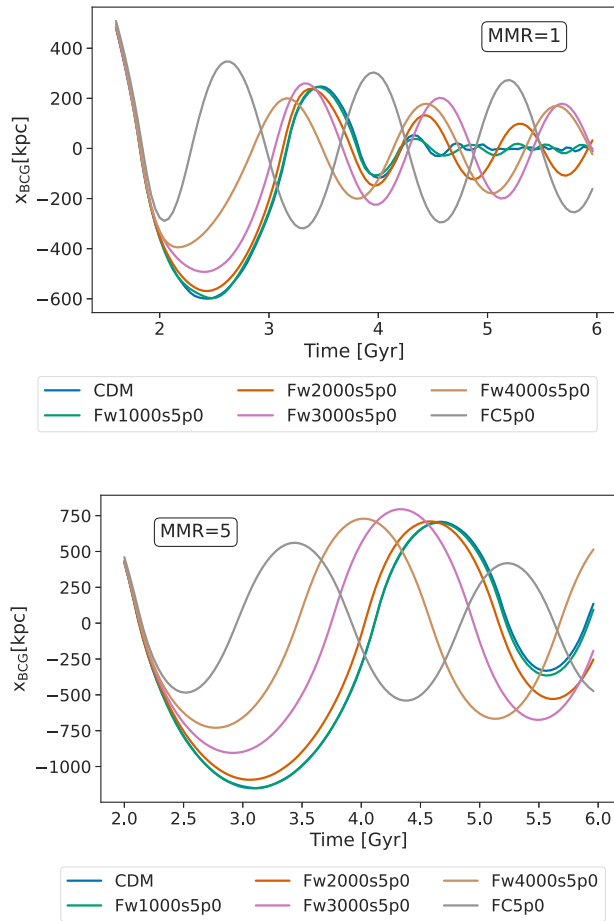


Figure 3. BCG position of the subhalo versus time. The upper panel shows peak positions in the equal-mass merger, while the lower panel corresponds to the unequal-mass merger. For better visibility, we plot only the position of the BCG of the subhalo. Plot labels are described in Table 3.

constant amplitude, and they have significantly deviated from the CDM simulation. The typical velocities around the DM peak at various stages of the evolution are given in Fig. D2. The central relative velocity dispersion around the DM peak is large at the first pericentre owing to the active merging. At later stages, when the haloes have slowed down, they have a very slowly rising relative velocity dispersion for the rest of the simulated time period. Therefore, from Fig. 1 we see that for $w = 2000 \text{ km s}^{-1}$ and $v > 2000 \text{ km s}^{-1}$, the σ_T is less than $1 \text{ cm}^2 \text{ g}^{-1}$, whereas for $v < 2000 \text{ km s}^{-1}$ the cross-section is larger than $1 \text{ cm}^2 \text{ g}^{-1}$. Thus, merger remnants experience larger self-interactions at later stages, leading to more cored distributions and lesser dynamical friction. Cumulatively, this leads to steady oscillations at later stages.

The distance travelled by the BCGs at the first apocentre is observed to become smaller with increasing values of w . This can be understood by looking at the DM peaks. For example, the DM haloes coalesce at the first pericentre passage for the constant σ_T simulation. As a result, the BCG experiences a larger gravitational force due to the coalesced DM distribution at the barycentre. This accumulation of DM at the barycentre reduces with decreasing w since the average interaction strength reduces with w . This effectively leads to smaller amplitudes at the first apocentre in both equal and unequal-mass mergers. Immediately after the second pericentre passage, the amplitude of the velocity-dependent SIDM and CDM

curves have decreased significantly due to dynamic friction. In the constant σ_T simulation, the DM peaks have come to rest, and the merger remnants start coring. This leads to the persistence of the BCG oscillation amplitude.

3.3 Morphology

In Fig. 4, we show the physical density of DM within the slice $|z| < 100 \text{ kpc}$ projected on the merger plane. There are three columns, each correspond to a DM model and each row corresponds to a particular simulation time. First we look at time $t = 1.4 \text{ Gyr}$, i.e. before the first pericentre passage. Both haloes in the constant σ_T simulation (column 2) have lower central densities than in the CDM (column 1) and velocity-dependent simulations (column 3). The second row shows results at a time $t = 2.1 \text{ Gyr}$, which is just after the first pericentre passage. Owing to the large self-interaction strength, the haloes in the constant σ_T simulation have coalesced, while for CDM and velocity-dependent self-interactions the DM haloes pass through each other. At later stages, $t > 5 \text{ Gyr}$, the merger remnant in the constant σ_T simulation has a lower central density. While for the velocity-dependent simulations, the effects of velocity-dependence slowly becomes relevant as the system slows down. Thus, this leads to more cored distribution at the centre of the merger remnant when compared to the one from CDM simulation. This feature essentially leads to the persistent BCG oscillations at late stages. In Fig. 5 we have a similar plot displaying only the subhalo's projected density for MMR:5. Independent of the choice for the $\sigma_T(v)$, the subhaloes are observed to evaporate with time. With self-interactions, the evaporation is more pronounced. At $t = 4.5 \text{ Gyr}$, the subhalo experiencing constant σ_T has its core dissolved significantly and comes to rest. For CDM, the core has remained relatively intact. Finally, in the velocity-dependent simulation, the core has dissolved. Although the merger remnant seems to be oscillating even at these stages. In addition, in the CDM simulation, we see shell-like features. These features are missing in the constant σ_T simulation, since the haloes have coalesced.

4 CENTRAL DENSITY MATCHED CROSS-SECTION

In this section, we explore a more refined matching procedure based on simulations of isolated haloes. In this matching scheme, parameters $\{\sigma_{0m}, w\}$ are chosen such that different parameter combinations lead to similar central density evolution. We will refer to parameters matched according to this scheme as CD-matched. To avoid performing multiple simulations to find the matched parameter set, we make use of the self-similar nature of the gravothermal fluid equations of an isolated halo (Balberg, Shapiro & Inagaki 2002; Essig et al. 2019). This allows us to obtain the central density evolution without running a suite of simulations. In Balberg, Shapiro & Inagaki (2002), they assume that the total cross-section is velocity independent. In order to illustrate the rescaling, consider two constant cross-section parameters $\sigma_{0m}^A, \sigma_{0m}^B$. Then, the central density evolution obeys the following scaling relation:

$$\rho_c(t^A) = \rho_c \left(t^B \times \frac{\sigma_{0m}^B}{\sigma_{0m}^A} \right), \quad (9)$$

where t^A, t^B correspond to the evolution time of the isolated haloes simulated with parameters $\sigma_{0m}^A, \sigma_{0m}^B$.

Velocity-dependent cross-sections contain two parameters, and it is not immediately clear how the central densities can be rescaled. Yang & Yu (2022) propose an effective cross-section σ_{eff} to model

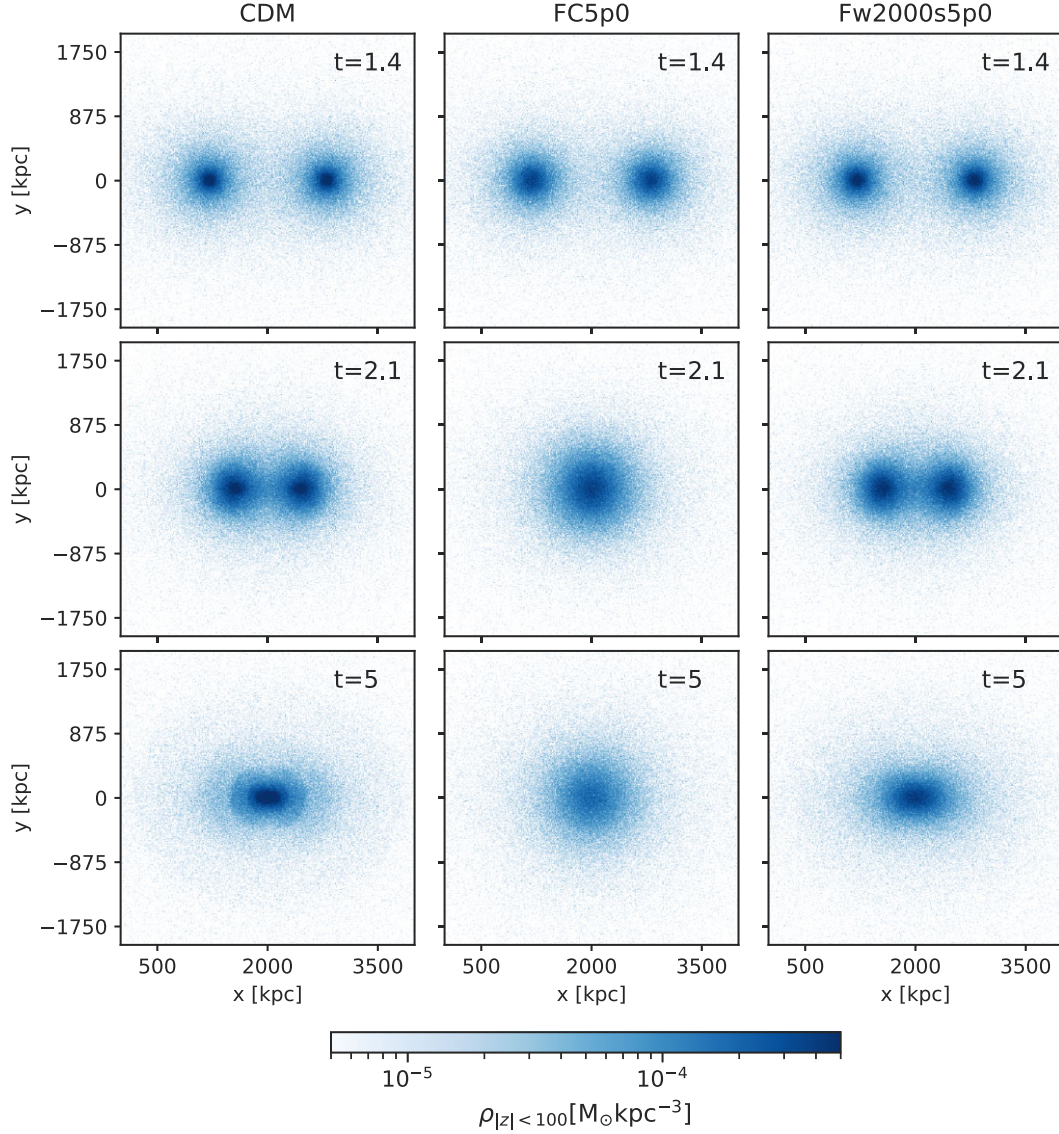


Figure 4. The density of DM haloes, accounting for the particles within $|z| < 100$ kpc. The first column corresponds to CDM simulations, while the second and the third columns correspond to simulations with the following momentum transfer cross-sections (σ_{0m}, w) : $(5, \infty)$, $(5, 2000)$. The rows correspond to different times. The first row being before the pericentre passage, the second, just after the first pericentre passage and the third being at later stages. The time stamps in the images are in units of Gyr.

the halo evolution. For a differential cross-section $d\sigma/d\cos\theta$, the effective cross-section is given by

$$\sigma_{\text{eff}} = \frac{1}{512(\sigma_{\text{1D}})^8} \int v^2 dv d\cos\theta v^5 \sin^2\theta \frac{d\sigma}{d\cos\theta} \exp\left(-\frac{v^2}{4\sigma_{\text{1D}}^2}\right). \quad (10)$$

In the expression given above, v is the relative velocity of DM particles, σ_{1D} is the characteristic velocity dispersion of the halo. Yang & Yu (2022) show that the evolution of central density in a simulation with the differential cross-section can be mimicked by a constant cross-section simulation with the same σ_{eff} . They also note that the equivalence holds well when the halo is in short-mean-free-path regime. In the long-mean-free-path regime, σ_{eff} does not capture the effects of self-scattering accurately. However, it provides a reasonable approximation to the halo evolution. Therefore, we extend the rescaling procedure given in equation (9) to any differential cross-section by using the corresponding effective cross-section σ_{eff} .

Integrating the angular part of equation (10), we get

$$\sigma_{\text{eff}} \propto \int v^2 dv v^5 \sigma_{\text{v}}(v, w) \exp\left(-\frac{v^2}{4\sigma_{\text{1D}}^2}\right) \propto \sigma_{0m} f(w), \quad (11)$$

where

$$\sigma_{\text{v}} = \int d\cos\theta \sin^2\theta \frac{d\sigma}{d\cos\theta}, \quad (12)$$

is the viscosity cross-section.

Thus, for a given w , $\sigma_{\text{eff}}^A/\sigma_{\text{eff}}^B = \sigma_{0m}^A/\sigma_{0m}^B$. In other words, rescaling by σ_{eff} is equivalent to rescaling by σ_{0m} for the same w . We verify this method by performing tests with some parameter combinations, see Appendix B.

In order to find the value σ_{0m} given a w , such that the evolution of the central density matches that of a target simulation with parameter set, $Q = \{\sigma_{0m}^Q, w^Q\}$ we follow the procedure given below.

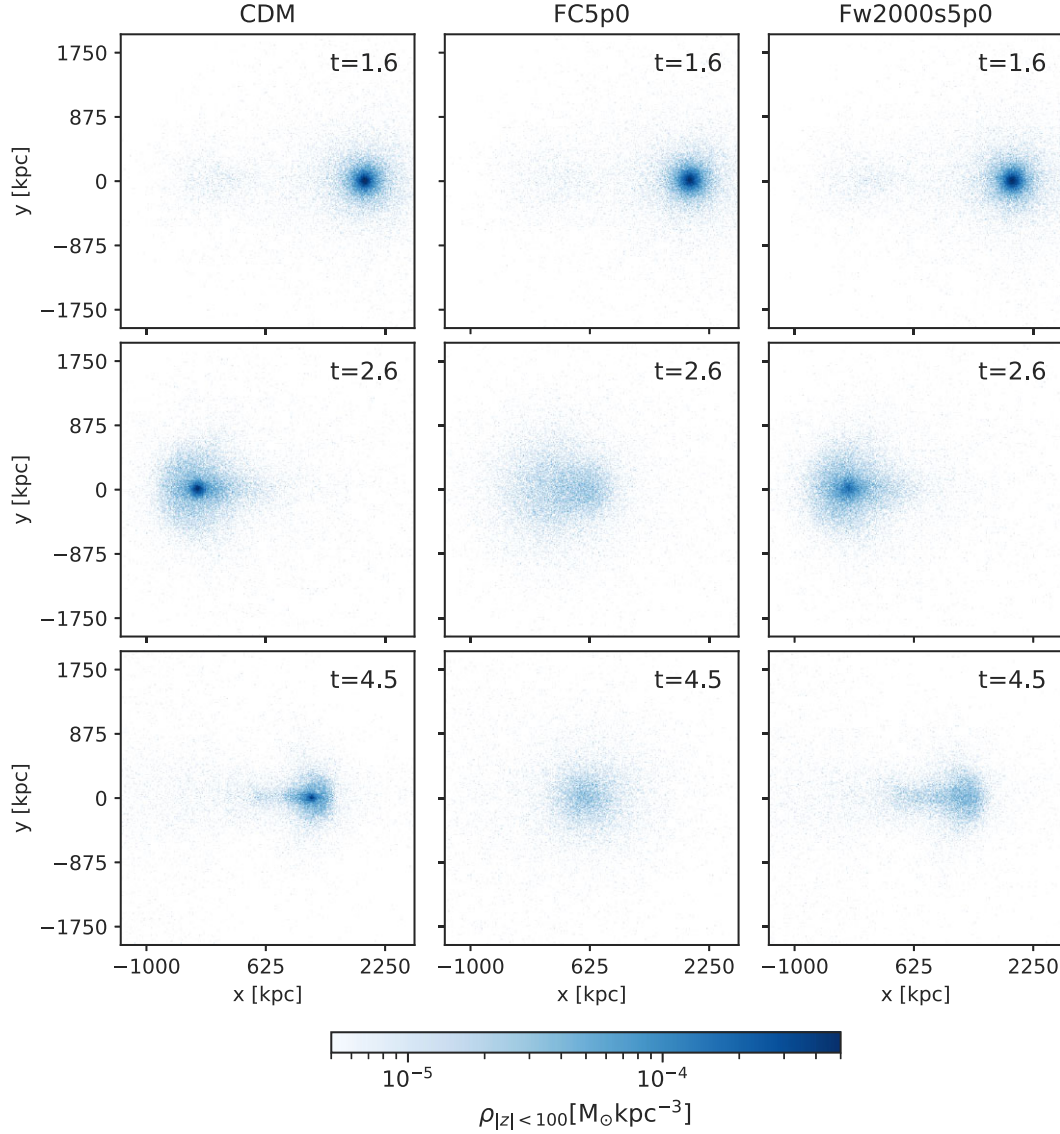


Figure 5. Plot similar to Fig. 4, but displaying only the subhalo of MMR:5 simulation.

(i) Simulate an isolated halo with the target parameter set. Find the evolution of the central density $\rho_c^Q(t^Q)$ from the simulation snapshots.

(ii) Simulate an isolated halo with the parameter set $A = \{\sigma_{0m}^A, w\}$, followed by the estimation of the evolution of central density $\rho_c^A(t^A)$ from the simulation data.

(iii) To obtain the evolution $\rho_c^B(t^B)$ corresponding to the parameter set $B = \{\sigma_{0m}^B, w\}$, rescale the time axis of the simulation A, i.e.

$$\rho_c^B(t^B) = \rho_c^A \left(t^A \times \frac{\sigma_{0m}^A}{\sigma_{0m}^B} \right). \quad (13)$$

(iv) Repeat the previous step with different values of σ_{0m}^B until $\rho_c^B(t^B)$ matches $\rho_c^Q(t^Q)$.

Thus, we have obtained the CD-matched σ_{0m}^B for the given w .

To make a guess for the value of σ_{0m}^A for one of our chosen values of w , we solve,

$$\sigma_{\text{eff}}(\sigma_{0m}^A, w) = \sigma_{\text{eff}}^Q. \quad (14)$$

To this end, we need a value for σ_{1D} . In Yang & Yu (2022), they propose to use the velocity dispersion in the central region of the halo at the maximal core expansion stage for the characteristic dispersion σ_{1D} . Using semi-analytic modelling, Outmezguine et al. (2023) show that the 1D velocity dispersion is $0.64V_{\text{max}}$ at the maximal core expansion phase. Using $V_{\text{max}} \approx 1.65r_s\sqrt{G\rho_0}$ for our NFW parameters, we find $\sigma_{1D} \approx 980 \text{ km s}^{-1}$. On the other hand, we observe $\sigma_{1D} \approx 1000 \text{ km s}^{-1}$ in our simulations. Thus, we find consistency between our simulations and the semi-analytic result.

We calculate the initial guess σ_{0m}^A for rare self-interactions and use the same for frequent self-interactions. For this calculation, we use the differential cross-section given in Section 2.3.

We choose the target set Q to correspond to the values quoted in Sagunski et al. (2021). They quoted a 95 per cent upper limit on σ/m_χ of $0.35 \text{ cm}^2 \text{ g}^{-1}$, assuming isotropy and velocity independence. Therefore, this value translates to $\sigma_{0m} = 0.175 \text{ cm}^2 \text{ g}^{-1}$ for rare self-interactions (because $\sigma = 2\sigma_T$). In other words, we choose the target set $Q = \{0.175 \text{ cm}^2 \text{ g}^{-1}, \infty\}$. In Fig. 6, we show an example for the matching procedure in detail. The black band corresponds to the target central density of constant σ_T with $\sigma_{0m} = 0.175 \text{ cm}^2 \text{ g}^{-1}$.

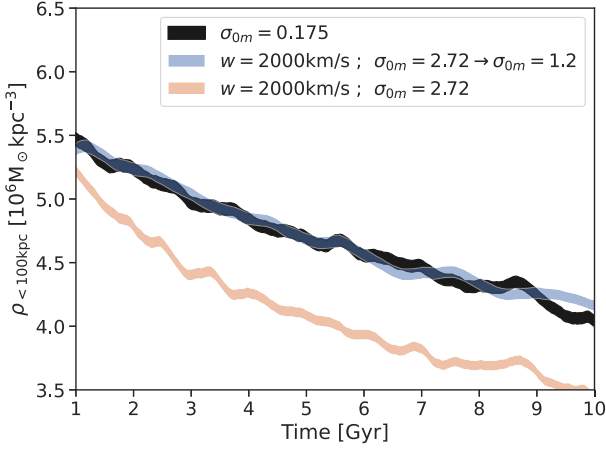


Figure 6. Evolution of central density of an isolated halo of virial mass $10^{15}M_{\odot}$. There are three bands in the plot corresponding to, (i) simulation with rare self-interactions with constant σ_{τ} of $\sigma_{0m} = 0.175$ (ii) simulation for $w = 2000 \text{ km s}^{-1}$ with an initial guess of $\sigma_{0m} = 2.72 \text{ cm}^2 \text{ g}^{-1}$ (iii) the same simulation as the earlier one, but rescaled to $\sigma_{0m} = 1.2 \text{ cm}^2 \text{ g}^{-1}$. The width of the band corresponds to the uncertainty in the estimation of central density, and it is proportional to $1/\sqrt{N}$.

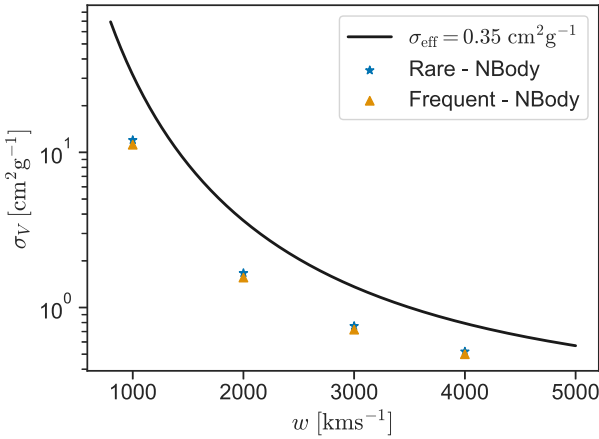


Figure 7. The plot contains viscosity cross-section evaluated at $v = 0$, for different values of w . At each w , the inferred value of σ_{0m} is used to compute σ_v . The triangles and stars represent σ_v calculated using the σ_{0m} inferred from N -body simulations for fSIDM and rSIDM, respectively. The solid line corresponds to σ_{0m} inferred by solving $\sigma_{\text{eff}} = 0.35 \text{ cm}^2 \text{ g}^{-1}$.

The orange band corresponds to a simulation with $\{2.72 \text{ cm}^2 \text{ g}^{-1}, 2000 \text{ km s}^{-1}\}$. This value for σ_{0m} is our initial guess calculated using equation (14). After rescaling by trial and error, the desired value of σ_{0m} is found to be $1.2 \text{ cm}^2 \text{ g}^{-1}$. This procedure can be extended to all chosen values of w and the obtained results are tabulated in Table 5. The inferred values of σ_{0m} at different values of w can then be used to calculate the corresponding viscosity cross-section σ_v . This is shown in Fig. 7. The orange triangles and blue stars represent the values of σ_v obtained using the inferred values of σ_{0m} from N -body simulations for rare and frequent self-interactions, respectively. Similarly, the solid line corresponds to the σ_v calculated from the values of σ_{0m} inferred by solving equation (14). The fact that the results obtained from σ_{eff} and N -body simulations are different can be attributed to the fact that the isolated halo is in the long-mean-free-path regime. This was already noted in Yang & Yu (2022).

The evolution of an isolated halo has a feature that, as long as it is in the core expansion phase, at any given time the central density is monotonically decreasing with σ_{eff} . This implies that for a given value of w , and at a given time in the evolution of the halo, core-size is larger for larger values of σ_{0m} . Andrade et al. (2021), Sagunski et al. (2021), and Eckert et al. (2022) constrain σ_{0m} using the observed core-size in clusters. Hence, for every value of w , there is a value of σ_{0m} that produces core sizes, or central densities, similar to the current upper bound. Increasing σ_{0m} any further would increase the core size to values larger than what is observed. Thus, this matching procedure can be used to extend the bounds from constant σ_{τ} to different values of w .

When matched using σ_{eff} or central density evolution, we observe that the ratio between the σ_{0m} 's of rare and frequent is approximately 0.64 at every chosen values of w . This can be understood from the definition of σ_{eff} . From equation (11), we have for any w , for rare self-interactions,

$$\sigma_{\text{eff}} = C\sigma_{0m} \int d\theta \sin^3 \theta \int dv v^7 \exp\left(\frac{-v^2}{4\sigma_{\text{ID}}^2}\right) \left(1 + \frac{v^2}{w^2}\right)^{-2} \quad (15)$$

$$= C \frac{4}{3} \sigma_{0m} f(w). \quad (16)$$

Here, $C = 1/(512\sigma_{\text{ID}}^8)$. Now from equation (6), for rare self-interactions we have $\sigma_{\tau} = \sigma_{0m}g(w, v)$, which implies that

$$\sigma_{\text{eff}} = \frac{4}{3} \sigma_{\tau} C f/g. \quad (17)$$

For frequent self-interactions, we consider a differential cross-section of the form given in equation (8) with the function $\Theta(\theta)$ having support only for values of θ close to 0. A simple choice for $\Theta(\theta)$ is a step-function that is non-zero in the interval $[0, \epsilon]$, where ϵ is some small number. Therefore, σ_{eff} is given as

$$\sigma_{\text{eff}} = CN\sigma_{0m} \int d\theta \sin^3 \theta \Theta(\theta) \int dv v^7 \exp\left(\frac{-v^2}{4\sigma_{\text{ID}}^2}\right) g(w, v) \quad (18)$$

$$\approx CN\sigma_{0m} \int d\theta \theta^3 \Theta(\theta) f(w) = CN\sigma_{0m} f(w)\epsilon^4/4, \quad (19)$$

where in the second equality we have Taylor-expanded and retained only the leading order in θ in the angular integrand. Similarly, for the momentum transfer cross-section we have

$$\sigma_{\tau} = N\sigma_{0m}g(w, v) \int d\theta \sin \theta (1 - |\cos \theta|) \Theta(\theta) \quad (20)$$

$$\approx N\sigma_{0m}g(w, v)\epsilon^4/8. \quad (21)$$

Thus for frequent self-interactions, we have

$$\sigma_{\text{eff}} = 2\sigma_{\tau} C f/g. \quad (22)$$

Now for matching with σ_{eff} or the central density we require $\sigma_{\text{eff}}(\text{Rare}) = \sigma_{\text{eff}}(\text{Freq.})$. Upon using equation (17) and equation (22), this requirement leads to the matching condition $\sigma_{\tau}(\text{Freq.}) = (2/3)\sigma_{\tau}(\text{Rare}) \Rightarrow \sigma_{0m}(\text{Freq.}) = (2/3)\sigma_{0m}(\text{Rare})$ as seen in Table 5.

4.1 Central density matched simulations – qualitative features

In this subsection, we look at the qualitative differences in mergers when parameters are chosen according to the central density matching procedure. Again, as in Section 3, we only simulate frequent self-interactions. In Section 3, we investigated the effects arising from changing the value of w . To ensure that the effects of self-interaction are not negligible for $w = 1000 \text{ km s}^{-1}$, we used a large value for σ_{0m} of $5.0 \text{ cm}^2 \text{ g}^{-1}$. On the other hand, in this section the cross-section parameters are CD-matched for which we choose the

Table 4. This table contains labels and cross-section parameters matched to constant cross-section, $\sigma_{0m} = 1.0 \text{ cm}^2 \text{ g}^{-1}$ of frequent self-interactions using central density matching scheme.

w (km s^{-1})	σ_{0m} ($\text{cm}^2 \text{ g}^{-1}$)	Label
1000	70.0	Fw1000s70p0
2000	8.67	Fw2000s8p67
3000	3.67	Fw3000s3p67
4000	2.33	Fw4000s2p33
∞	1.0	FC1p0

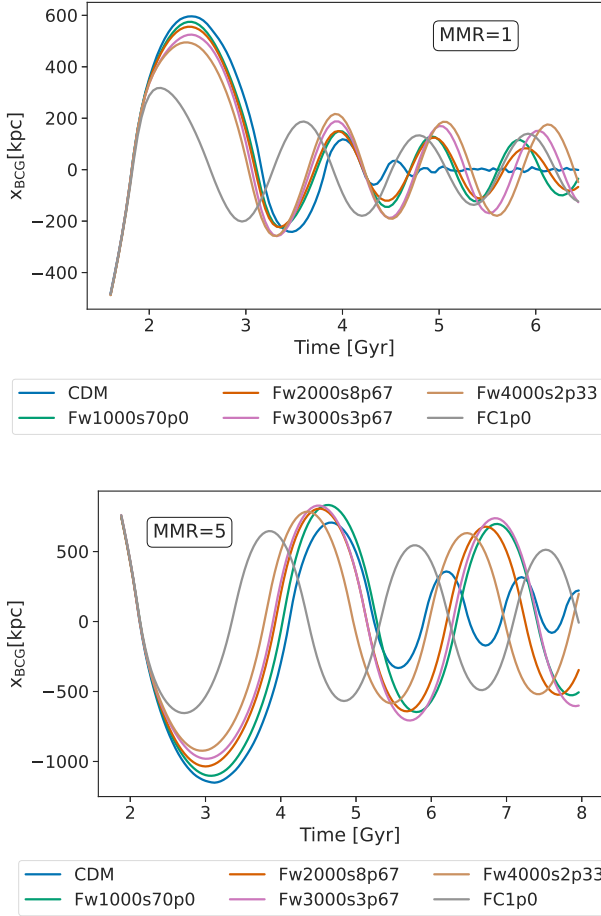


Figure 8. BCG positions of the subhalo against time. The upper panel corresponds to equal mass merger, while the lower one corresponds to unequal mass merger.

target set to be $Q = \{1.0 \text{ cm}^2 \text{ g}^{-1}, \infty\}$. The matched parameters are given in Table 4. We have chosen a value for σ_{0m} such that the effects of self-interaction are observable, but not as large as the previous value $5.0 \text{ cm}^2 \text{ g}^{-1}$.

For brevity, we show only the BCG oscillations in Fig. 8. We see that the BCG oscillations of velocity-dependent simulations all have similar amplitudes at early stages. Only at a later stages they start to deviate. This similarity stems from the fact that the parameters are CD-matched. Similar to what was explained in Section 3.2, at early times the DM particles have a large relative velocity. As a result, most of the velocity-dependent cross-sections have a small effective self-interaction strength. At later stages, the system slows down and $v \lesssim w$ and the effective self-interaction strength increases.

Table 5. This table contains the conservative upper bound on σ_{0m} for different values of w given in the first column. The second column contains σ_{0m} the value for frequent self-interactions, and the third for rare self-interactions.

w (km s^{-1})	Frequent		Rare	
	σ_{0m} ($\text{cm}^2 \text{ g}^{-1}$)	Label	σ_{0m} ($\text{cm}^2 \text{ g}^{-1}$)	Label
1000	5.6	Fw1000s5p6	9.0	Rw1000s9p0
2000	0.78	Fw2000s0p78	1.25	Rw2000s1p25
3000	0.36	Fw3000s0p36	0.57	Rw3000s0p57
4000	0.25	Fw4000s0p25	0.39	Rw4000s0p39
∞	0.11	FC0p11	0.175	RC0p175

In addition, the internal evolution around a DM peak is similar for all the cross-section parameters chosen, since they are CD-matched. See appendix C for the evolution of the central density of the main halo.

4.2 Central density matched upper bound simulations

In Section 4, the conservative upper bounds were obtained using the central density matching scheme. Values are tabulated in Table 5. We run merger simulations for this set of parameters and estimate the offsets $d_{\text{DM-BCG}}$. For velocity-independent cross-sections up to $0.5 \text{ cm}^2 \text{ g}^{-1}$, Fischer et al. (2021) found that the DM-BCG and DM-Galaxy offsets increase with increasing values of σ_{0m} . By running merger simulations at the upper bound values of the cross-section parameters, we estimate the order of magnitude of the largest possible offsets allowed by current bounds.

In Fig. 9, we show the DM-BCG offset at the first pericentre passage for the equal mass merger. The offset is $\mathcal{O}(1)\text{kpc}$, while the offsets after the third pericentre passage ($t \sim 4$ billion years) start increasing and is seen to be $\mathcal{O}(10)\text{kpc}$. The effective self-interaction strength is not large enough to produce an observable offset at the first pericentre. Hence, it might be difficult to find such an offset in real observations. We do not show the offsets for unequal mass merger because, the offsets just after the first pericentre are smaller than the ones of equal mass merger. In addition, at later stages due to the evaporation of halo, we do not have reliable peak positions. We can also see from Fig. 9 that the offsets produced by fSIDM are larger than that of rSIDM, and this is due to the fact that mergers are sensitive to the angular dependence.

5 CONCLUSIONS

We first discuss the assumptions made in the paper before we conclude. The first assumption that we make is that we use idealized initial conditions. Yet, it is informative to study them to find the appropriate features to look out for in more realistic simulations and observations. One example is the amplitude of BCG oscillation at late stages, which is seen to depend on the velocity-dependent cross-section parameters. Therefore, it is instructive to simulate cosmological boxes with velocity-dependent cross-section at higher resolution in order to estimate the distribution of DM-BCG offsets. Later, this could be compared to observations (e.g. Lauer et al. 2014; Cross et al. 2023). For example, Harvey et al. (2019) studied the DM-BCG offsets in the BAHAMAS-SIDM suite of cosmological simulations and placed constraints on σ/m_χ assuming velocity-independent isotropic SIDM.

In addition, we have modelled the BCG and galaxies as collisionless point particles. A more realistic treatment of BCG's and galaxies

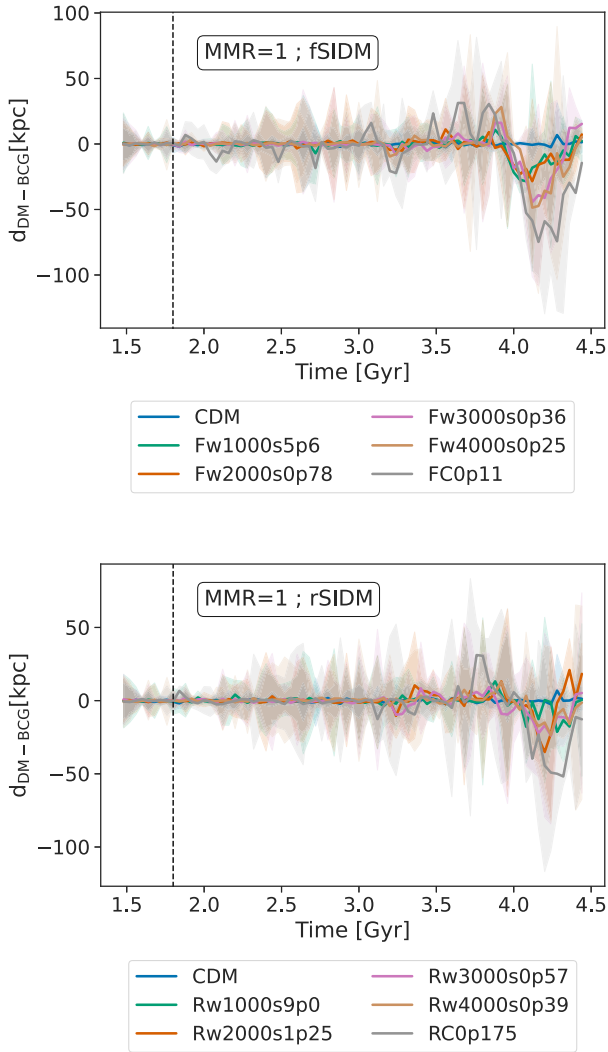


Figure 9. DM–BCG offsets in the equal-mass merger. Upper panel corresponds to fSIDM, while bottom panel to rSIDM. The plot labels are described in Table 5. The vertical dashed lines correspond to the time of the first pericentre passage.

is necessary for better comparison with observations. Furthermore, we neglect the effect of galaxies having their own DM halo (Kummer, Kahlhoefer & Schmidt-Hoberg 2018). In reality, approximately 10 per cent of the mass of clusters is made up by the intracluster medium (ICM), which is not included in our simulations. Merger studies that include the ICM, such as Robertson, Massey & Eke (2017a), find that the DM–galaxy offset is not significantly affected by the presence of the ICM. Fischer et al. (2023) also finds similar results. Therefore, we argue that the absence of an ICM component does not significantly affect our conclusions. We leave the study of these systems with hydrodynamic simulations to a future study.

As mentioned in Section 2.3, we have assumed that the angular and velocity dependence of the differential cross-sections can be separated into two functions. This assumption has to be dropped when dealing with realistic SIDM models (Feng et al. 2009; Tulin, Yu & Zurek 2013). There are other SIDM models leading to different effects that are not included in our studies. For example, in addition to elastic scattering, inelastic scattering could be included (O’Neil et al. 2023). We leave the study of such models to future work.

On the observation side, all observed DM–BCG offsets are inferred to be just after pericentre passage and have uncertainties that make them consistent with zero (Bradač et al. 2008; Dawson et al. 2012; Dawson 2013; Jee et al. 2014, 2015). Similarly, estimating DM–galaxy offsets are difficult due to shot noise arising from the smaller galaxy count. In our simulations we had 10^6 galaxy particles, but in reality we observe at most $\sim 10^3$ of them. On the other hand, Lauer et al. (2014) find a median offset of ~ 10 kpc, with the offset measured between BCG and cluster centre, the latter being identified by X-ray observations. Their sample comprised 433 BCGs that are located in Abell galaxy clusters. The DM–BCG offset distribution could be compared to predictions of cosmological simulations. Overall, the situation with observations is expected to improve with forthcoming surveys, such as *SuperBIT* (Romualdez et al. 2016) and *Euclid* (Laureijs et al. 2011).

We have simulated idealized, isolated haloes and galaxy cluster mergers with equal and unequal merger mass ratios with velocity-dependent, frequent, and rare self-interactions. Mergers are interesting astrophysical probes since the system is sensitive to self-interaction cross-sections with both angular and velocity dependencies. Therefore, we focused on understanding the qualitative effects that arise from velocity dependence in mergers. On the quantitative side, we also investigate the maximum offsets that can be observed given the current bounds on σ/m_χ .

(i) Independent of the matching procedure used in the paper, the effects of velocity-dependent cross-sections can be observed on galaxy cluster mergers by comparing the early time and late time oscillations of BCG. In particular, the degeneracy in the cross-section parameters when studying the evolution of central density in isolated haloes is broken when studying mergers. This is due to the fact that the relative velocities of the merging clusters change with time.

(ii) The evolution of central densities of isolated haloes are similar between rare and frequent self-interaction, when the momentum transfer cross-section $\sigma_T(v)$ of fSIDM is chosen to be $2/3\sigma_T(v)$ of rSIDM. The factor $2/3$ follows from matching the angular dependence of fSIDM and rSIDM with viscosity cross-section, as seen in Fig. 7.

(iii) We extend the existing upper bounds on the constant cross-section σ_{0m} to the parameter space $\{\sigma_{0m}, w\}$ of velocity-dependent, rare, and frequent self-interactions.

(iv) In the equal-mass merger simulations with upper-bound cross-section parameters, we find that the offsets after the first pericentre is approximately $\mathcal{O}(1)$ kpc. In particular, the offsets are the largest in the constant cross-section simulation. As the system evolves further, offsets grow. After the third pericentre passage, due to the oscillations of BCG, and the galactic component the offsets are $\mathcal{O}(10)$ kpc. Thus, mergers in their late stages are interesting to test and constrain SIDM.

In conclusion, we have studied the qualitative effects of velocity-dependent SIDM cross-sections in galaxy cluster mergers. Our models do not have the realism required for a direct comparison with astronomical data, owing to the neglect of baryonic effects. However, they offer insights into the physical processes that govern the phenomenology of SIDM. More realistic predictions can be obtained by performing full hydrodynamical simulations that include stars, cooling, and feedback effects. The significantly larger complexity of such models with additional degrees of freedom render the interpretation much harder. Clearly, this is an avenue for future work.

ACKNOWLEDGEMENTS

We want to thank the anonymous referee for helpful comments that improved the paper. We would also like to thank all participants of the *Darkium* SIDM Journal Club for helpful discussions. This work is funded by the Deutsche Forschungsgemeinschaft (DFG, German Research Foundation) under Germany’s Excellence Strategy – EXC 2121 ‘Quantum Universe’ – 390833306, Germany’s Excellence Strategy – EXC-2094 ‘Origins’ – 390783311, and the Emmy Noether Grant No. KA 4662/1-2. Preprint numbers: DESY-23-153, TTP23-043.

DATA AVAILABILITY

The data underlying this article will be shared on reasonable request to the corresponding author.

REFERENCES

- Ackerman L., Buckley M. R., Carroll S. M., Kamionkowski M., 2009, *Phys. Rev. D*, 79, 023519
- Adhikari S. et al., 2022, Astrophysical Tests of Dark Matter Self-Interactions. preprint (arXiv:2207.10638)
- Andrade K. E., Fuson J., Gad-Nasr S., Kong D., Minor Q., Roberts M. G., Kaplinghat M., 2021, *MNRAS*, 510, 54
- Balberg S., Shapiro S. L., Inagaki S., 2002, *ApJ*, 568, 475
- Binney J., Tremaine S., 2008, *Galactic Dynamics: Second Edition*. Princeton Univ. Press, Princeton
- Boddy K. K., Feng J. L., Kaplinghat M., Tait T. M. P., 2014, *Phys. Rev. D*, 89, 115017
- Bradač M., Allen S. W., Treu T., Ebeling H., Massey R., Morris R. G., von der Linden A., Applegate D., 2008, *ApJ*, 687, 959
- Bullock J. S., Boylan-Kolchin M., 2017, *ARA&A*, 55, 343
- Cline J. M., Liu Z., Moore G. D., Xue W., 2014, *Phys. Rev. D*, 89, 043514
- Correa C. A., 2021, *MNRAS*, 503, 920
- Cross D. et al., 2023, Examining the Self-Interaction of Dark Matter through Central Cluster Galaxy Offsets. preprint (arXiv:2304.10128)
- Dawson W. A., 2013, PhD thesis, University of California, Davis
- Dawson W. A. et al., 2012, *ApJ*, 747, L42
- Dutton A. A., Macciò A. V., 2014, *MNRAS*, 441, 3359
- Eckert D., Ettori S., Robertson A., Massey R., Pointecouteau E., Harvey D., McCarthy I. G., 2022, *A&A*, 666, A41
- Elbert O. D., Bullock J. S., Garrison-Kimmel S., Rocha M., Oñorbe J., Peter A. H. G., 2015, *MNRAS*, 453, 29
- Essig R., McDermott S. D., Yu H.-B., Zhong Y.-M., 2019, *Phys. Rev. Lett.*, 123, 121102
- Feng J. L., Kaplinghat M., Tu H., Yu H.-B., 2009, *J. Cosmol. Astropart. Phys.*, 2009, 004
- Fischer M. S., Brüggem M., Schmidt-Hoberg K., Dolag K., Kahlhoefer F., Ragagnin A., Robertson A., 2021, *MNRAS*, 505, 851
- Fischer M. S., Brüggem M., Schmidt-Hoberg K., Dolag K., Ragagnin A., Robertson A., 2022, *MNRAS*, 510, 4080
- Fischer M. S., Kassermann L., Brüggem M., Dolag K., Kahlhoefer F., Ragagnin A., Robertson A., Schmidt-Hoberg K., 2024, preprint (arXiv:2310.07750)
- Fischer M. S., Durke N.-H., Hollingshausen K., Hammer C., Brüggem M., Dolag K., 2023, *MNRAS*, 523, 5915
- Gilman D., Bovy J., Treu T., Nierenberg A., Birrer S., Benson A., Sameie O., 2021, *MNRAS*, 507, 2432

- Harvey D., Massey R., Kitching T., Taylor A., Tittley E., 2015, *Science*, 347, 1462
- Harvey D., Robertson A., Massey R., McCarthy I. G., 2019, *MNRAS*, 488, 1572
- Jee M. J., Hughes J. P., Menanteau F., Sifón C., Mandelbaum R., Barrientos L. F., Infante L., Ng K. Y., 2014, *ApJ*, 785, 20
- Jee M. J. et al., 2015, *ApJ*, 802, 46
- Kahlhoefer F., Schmidt-Hoberg K., Frandsen M. T., Sarkar S., 2014, *MNRAS*, 437, 2865
- Kahlhoefer F., Schmidt-Hoberg K., Wild S., 2017, *J. Cosmol. Astropart. Phys.*, 2017, 003
- Kim S. Y., Peter A. H. G., Wittman D., 2017, *MNRAS*, 469, 1414
- Kummer J., Kahlhoefer F., Schmidt-Hoberg K., 2018, *MNRAS*, 474, 388
- Kummer J., Brüggem M., Dolag K., Kahlhoefer F., Schmidt-Hoberg K., 2019, *MNRAS*, 487, 354
- Lauer T. R., Postman M., Strauss M. A., Graves G. J., Chisari N. E., 2014, *ApJ*, 797, 82
- Laureijs R. et al., 2011, Euclid Definition Study Report. preprint (arXiv:1110.3193)
- Navarro J. F., Frenk C. S., White S. D. M., 1996, *ApJ*, 462, 563
- O’Neil S. et al., 2023, *MNRAS*, 524, 288
- Outmeuguine N. J., Boddy K. K., Gad-Nasr S., Kaplinghat M., Sagunski L., 2023, *MNRAS*, 523, 4786
- Randall S. W., Markevitch M., Clowe D., Gonzalez A. H., Bradač M., 2008, *ApJ*, 679, 1173
- Ren T., Kwa A., Kaplinghat M., Yu H.-B., 2019, *Phys. Rev. X*, 9, 031020
- Robertson A., Massey R., Eke V., 2017a, *MNRAS*, 465, 569
- Robertson A., Massey R., Eke V., 2017b, *MNRAS*, 467, 4719
- Rocha M., Peter A. H. G., Bullock J. S., Kaplinghat M., Garrison-Kimmel S., Oñorbe J., Moustakas L. A., 2013, *MNRAS*, 430, 81
- Romualdez L. J. et al., 2016, The Design and Development of a High-Resolution Visible-to-near-UV Telescope for Balloon-Borne Astronomy: SuperBIT. preprint(arXiv:1608.02502)
- Sagunski L., Gad-Nasr S., Colquhoun B., Robertson A., Tulin S., 2021, *J. Cosmol. Astropart. Phys.*, 2021, 024
- Sankar Ray T., Sarkar S., Kumar Shaw A., 2022, *J. Cosmol. Astropart. Phys.*, 2022, 011
- Spergel D. N., Steinhardt P. J., 2000, *Phys. Rev. Lett.*, 84, 3760
- Tulin S., Yu H.-B., 2018, *Phys. Rev.*, 730, 1
- Tulin S., Yu H.-B., Zurek K. M., 2013, *Phys. Rev. D*, 87, 115007
- Yang D., Yu H.-B., 2022, *J. Cosmol. Astropart. Phys.*, 2022, 077
- Yang S., Du X., Zeng Z. C., Benson A., Jiang F., Nadler E. O., Peter A. H. G., 2023, *ApJ*, 946, 47

APPENDIX A: VALIDATING LOWER RESOLUTION SIMULATIONS

In this section, we compare the peak positions of DM, galaxy, and BCG components between low resolution and high resolution simulations. The low- and the high-resolution simulation use the NFW parameters given in Table 1 for generating the haloes. The only difference being that the DM and galaxy particles in the high-resolution simulation have a resolution of 10^7 particles instead of 10^6 particles. Both of them also use the same initial conditions as given in Table 2. The DM component is simulated with and without self-interactions. For the SIDM case, we simulate with frequent self-interactions with a constant σ_T of $0.5 \text{ cm}^2 \text{ g}^{-1}$. We observe that the peak positions evolve almost identically independent of the resolution up until 5 billion years. See Figs A1 and A2.

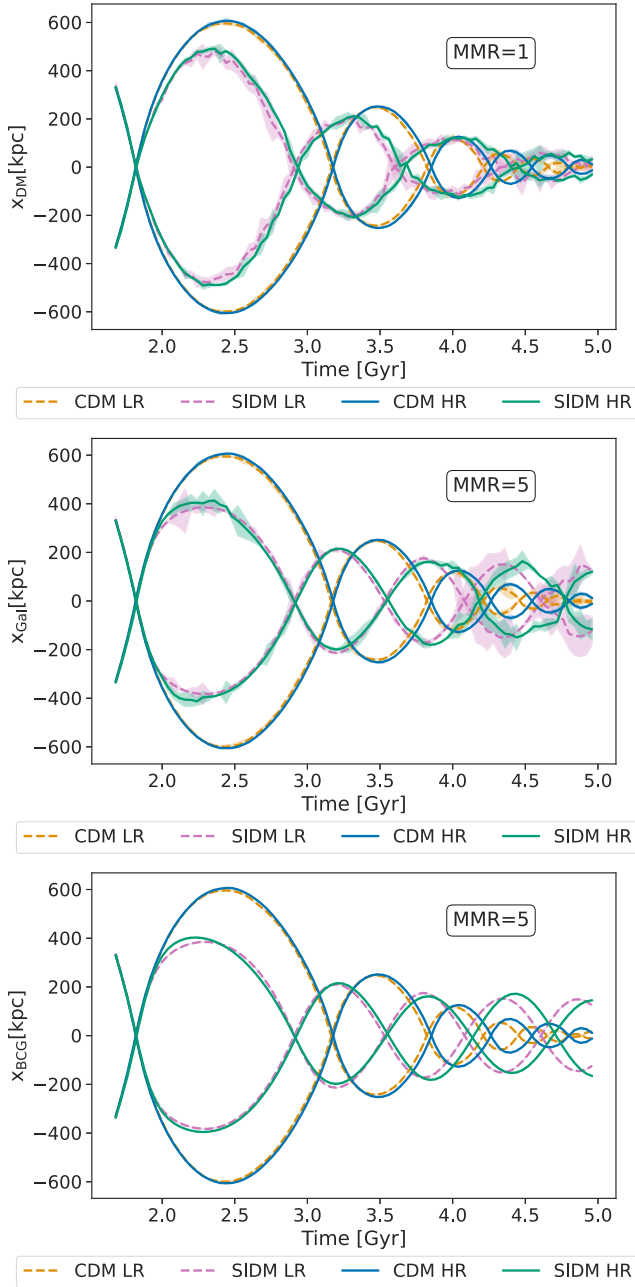


Figure A1. Comparison of peaks positions of different components between low and high resolutions for both CDM and SIDM simulations in the equal mass merger. Top, middle, and bottom panels correspond to DM, galaxy, and BCG components. The dashed lines correspond to low resolution and solid lines correspond to high resolution. The SIDM case corresponds to the frequent self-interactions with $\sigma_{0m} = 0.5 \text{ m}^2 \text{ g}^{-1}$.

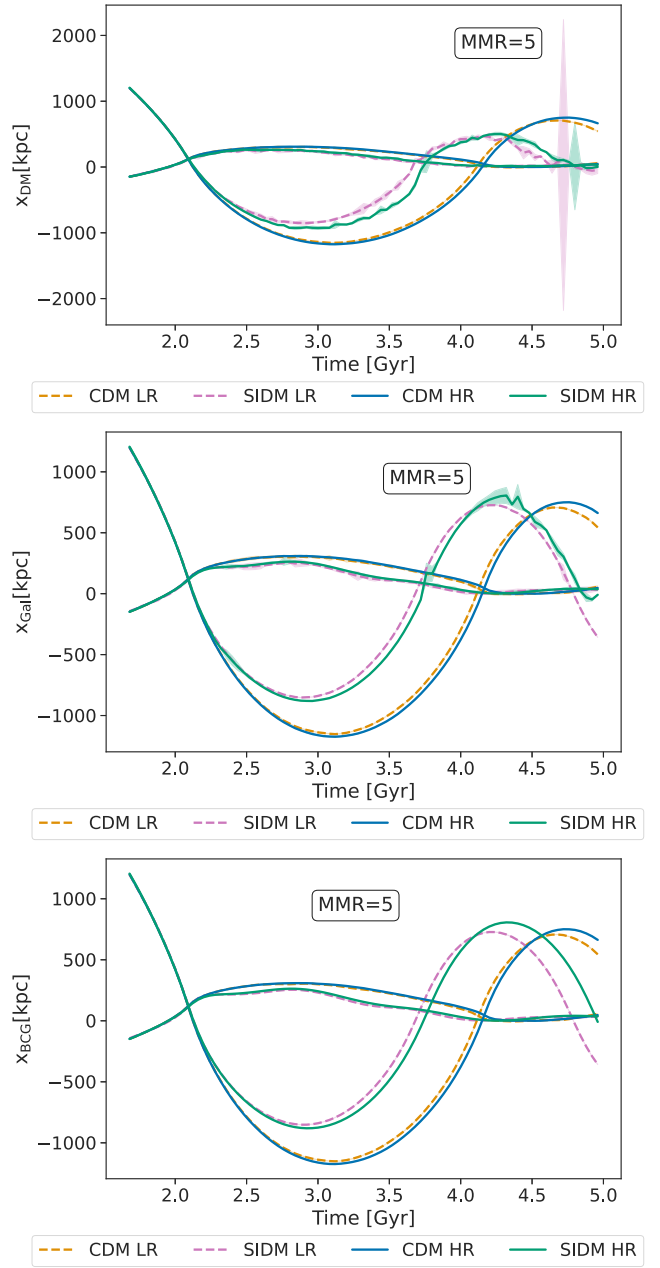


Figure A2. Comparison of peaks positions of different components between low and high resolutions for CDM and SIDM simulations in the unequal mass merger. Top, middle, and bottom panels correspond to DM, galaxy, and BCG components. The dashed lines correspond to low resolution and solid lines correspond to high resolution. The SIDM case corresponds to the frequent self-interactions with $\sigma_{0m} = 0.5 \text{ m}^2 \text{ g}^{-1}$.

APPENDIX B: TESTING RESCALING

We test the rescaling by σ_{0m} for a given w with rare self-interactions. Fig. B1 shows the evolution of central density of an isolated halo for two values of w – 2000 km s⁻¹ and 3000 km s⁻¹ – in the left and right panel, respectively. For example, in the left panel, after rescaling t of $\sigma_{0m} = 20$ cm² g⁻¹ simulation by a factor 20/13, the evolution is similar to the simulation with $\sigma_{0m} = 13$ cm² g⁻¹.

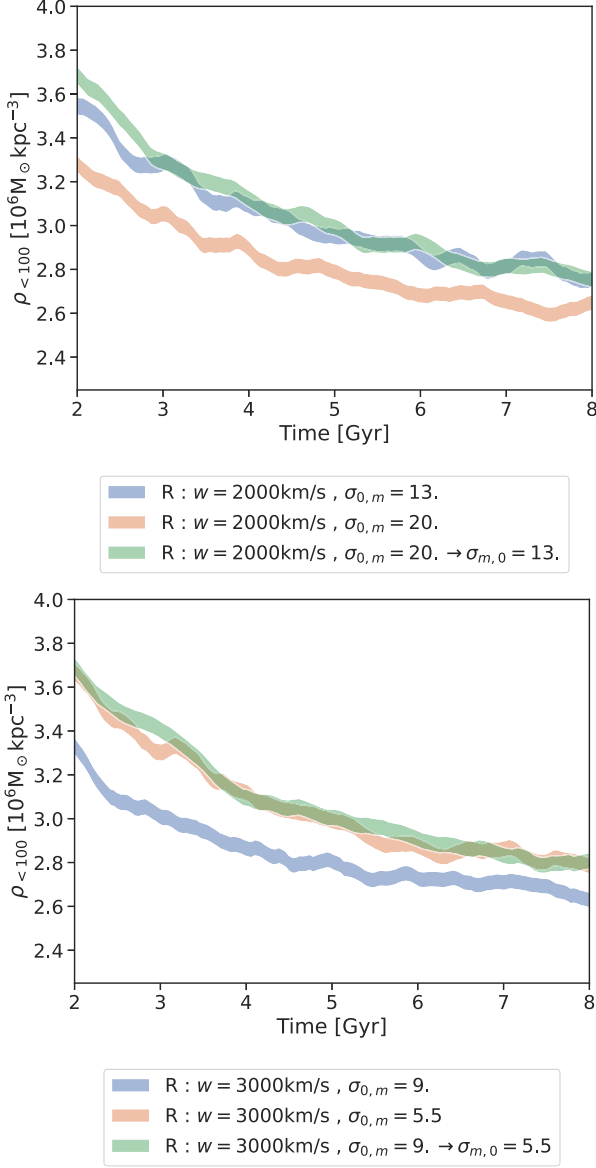


Figure B1. Evolution of central density for two values of w , 2000 and 3000 km s⁻¹ in the top and bottom panel, respectively.

APPENDIX C: CENTRAL DENSITY EVOLUTION IN MERGER

In Fig. C1, we show the evolution of the central density around the DM peak of the main halo in the equal mass merger. The curves

correspond to simulations where the cross-section parameters are CD-matched. Similarly, in Fig. C2 we show the central densities for cases when the cross-section parameters have the same σ_{0m} , but with varying w .

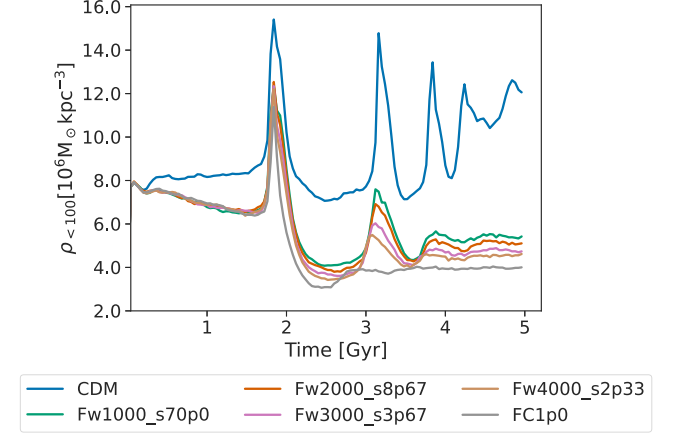


Figure C1. Evolution of the central density measured within 100 kpc around the DM peak of main halo. The parameters are CD-matched and the labels are explained in Table 4.

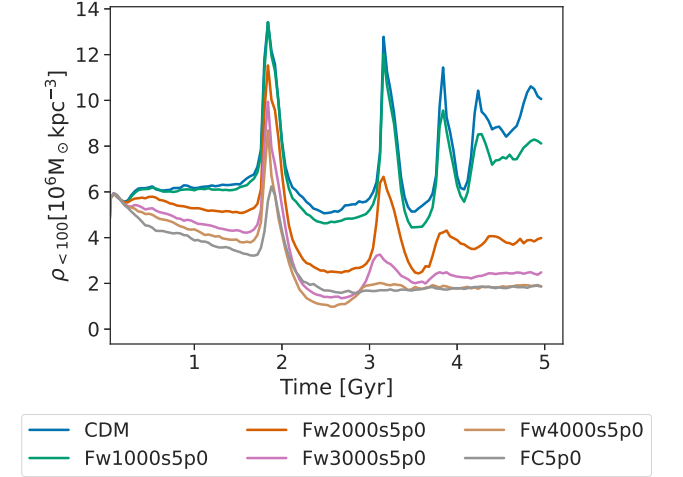


Figure C2. Evolution of the central density measured within 100 kpc, around the DM peak of main halo in the equal mass merger. The parameters have the same value of $\sigma_{0m} = 5$ cm² g⁻¹, but with varying values of w . The labels are explained in Table 3.

APPENDIX D: CENTRAL VELOCITY DISPERSION EVOLUTION IN MERGER

The relative velocity dispersion around the DM peak within 100 kpc in the equal mass merger is shown as a function of time in Figs D1 and D2. The earlier figure corresponds to simulations with cross-section parameters that are CD-matched, while the latter figure corresponds to cross-section parameters with fixed σ_{0m} and varying w . The relative velocity dispersion is calculated from the 1D velocity dispersion, i.e. $\sigma_{\text{rel}} = \sqrt{2}\sigma_{1D}$.

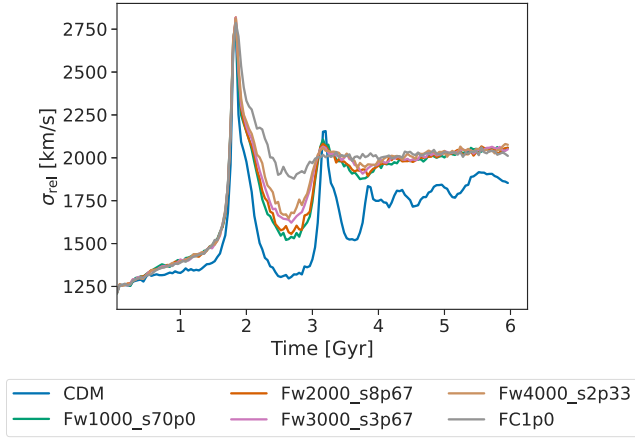


Figure D1. Evolution of the central relative velocity dispersion measured within 100 kpc around the DM peak of main halo. The parameters are CD-matched and the labels are explained in Table 4.

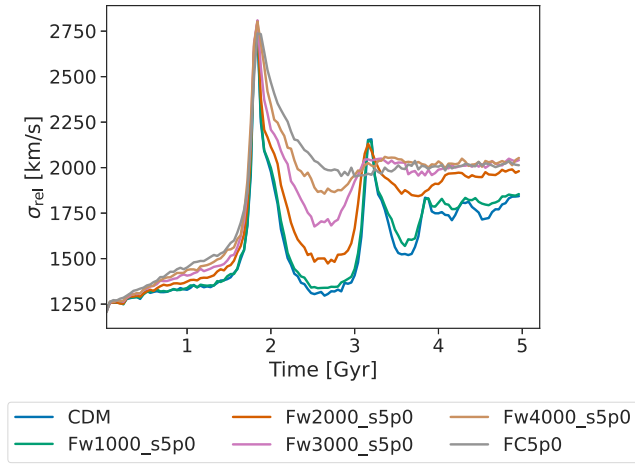


Figure D2. Evolution of the central relative velocity dispersion within 100 kpc around the DM peak of the main halo. The parameters have the same value of $\sigma_{0m} = 5 \text{ cm}^2 \text{ g}^{-1}$, but with varying values of w . The labels are explained in Table 3.

APPENDIX E: MOMENTUM TRANSFER CROSS-SECTION OF CD-MATCHED PARAMETERS

Plots similar to Fig. 1 but with CD-matched parameters are provided. Figs E1 and E2 correspond to the parameters in Tables 4 and 5, respectively.

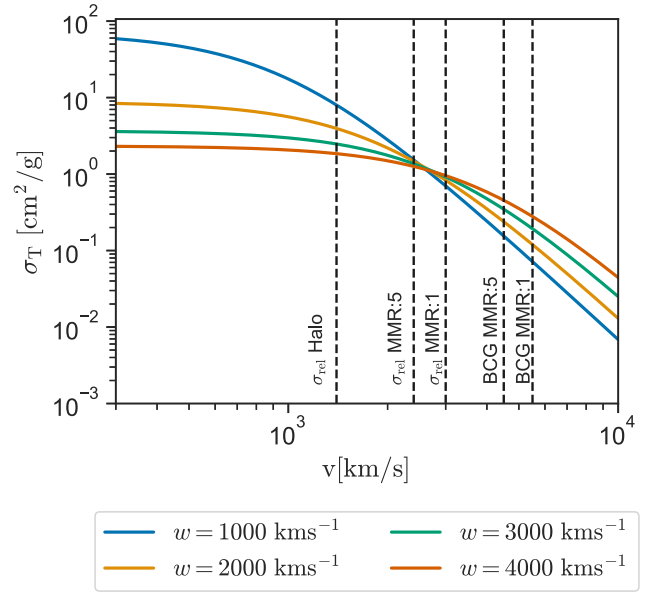


Figure E1. Momentum transfer cross-section as a function of velocity for the parameters given in Table 4. The vertical dashed lines are explained in the captions of Fig. 1.

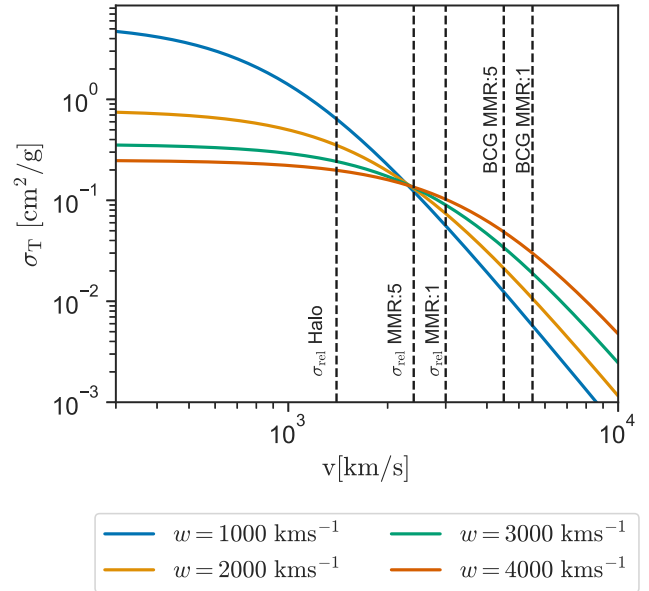


Figure E2. Momentum transfer cross-section as a function of velocity for the parameters given in Table 5. The vertical dashed lines are explained in the captions of Fig. 1.

This paper has been typeset from a $\text{\TeX}/\text{\LaTeX}$ file prepared by the author.